Author/s:
Desai, K;Li, R;Meighen-Berger, S

Title:
Searching for dark matter annihilation with IceCube and P-ONE

Date:
2024-02

Citation:
Desai, K., Li, R. & Meighen-Berger, S. (2024). Searching for dark matter annihilation with IceCube and P-ONE. Journal of Cosmology and Astroparticle Physics, 2024 (2), https://doi.org/10.1088/1475-7516/2024/02/049.

Persistent Link:
https://hdl.handle.net/11343/353971

Searching for dark matter annihilation with IceCube and P-ONE

Journal of Cosmology and Astroparticle Physics
An IOP and SISSA journal

Received: *July 10, 2023*
Revised: *December 22, 2023*
Accepted: *January 24, 2024*
Published: *February 26, 2024*

Searching for dark matter annihilation with IceCube and P-ONE

K. Desai[a], **R. Li**[a,b] **and S. Meighen-Berger**[a,c]

[a]*Ludwig Maximilian University, Geschwister-Scholl-Platz 1, 80539 München, Germany*
[b]*Technische Universität München, James-Franck-Straße, 85748, Garching, Germany*
[c]*School of Physics, The University of Melbourne, Melbourne, VIC 3010, Australia*

E-mail: desai.kruteesh@campus.lmu.de, ruohan.li@tum.de, stephan.meighenberger@unimelb.edu.au

Abstract: We present a new search for weakly interacting massive particles utilizing ten years of public IceCube data, setting more stringent bounds than previous IceCube analysis on massive dark matter to neutrino annihilation. We also predict the future potential of the new neutrino observatory, P-ONE, showing that it may even exceed the sensitivities of Fermi-LAT gamma-ray searches by about 1–2 orders of magnitude in 1–10 TeV regions. This analysis considers the diffuse dark matter self-annihilation to neutrinos via direct and indirect channels, from the galactic dark matter halo and extra-galactic sources. We also predict that P-ONE will be capable of pushing these bounds further than IceCube, even reaching the thermal relic abundance utilizing a galactic center search for extended run-time.

Keywords: dark matter simulations, neutrino detectors, neutrino experiments

ArXiv ePrint: 2302.10542

https://doi.org/10.1088/1475-7516/2024/02/049

JCAP02(2024)049

Contents

JCAP02(2024)049

1 Introduction

New neutrino telescopes under construction, such as P-ONE [1], KM3NeT [2], GVD [3], and IceCube-Gen2 [4], will improve the global sky coverage. This will lead to an increased detection sensitivity from both diffuse and point-like signals. With these new detectors in mind, we estimate neutrino telescope sensitivities to dark matter (DM) annihilation and set constraints using ten years of public IceCube data. Already, multiple dark matter studies using IceCube [5] and/or ANTARES [6] have been performed, such as the search for dark matter from the Galactic Center [7, 8], earth [9], Sun [10, 11], multi-messenger searches [12], and diffuse searches for decaying or interacting dark matter [13–18].

Here we consider Majorana weakly interacting massive particles (WIMPs) as dark matter candidates. In the case of dark matter self-annihilation to neutrino pairs, the spectrum would possess a distinct shape: a peak at the DM rest mass. This feature differs fundamentally from the measured diffuse astrophysical neutrino power-law spectrum [8, 19], as well as the atmospheric background. Due to this, we perform energy-binned likelihood analyses, searching for these exotic energy distributions.

In standard WIMP freeze-out scenarios, DM particles are assumed to be in thermal equilibrium, with the expanding universe, the dark sector decouples due to the expansion rate increasing greater than the interaction rate, ceasing DM production and self-interaction leading to the relic density [20–22]. In this scenario, to account for current DM observations, the thermally averaged annihilation cross section would then be $\langle\sigma\nu\rangle = 3\times10^{-26}$ cm^{3}s^{-1} [20]. Thus, should DM not be found, the searches aim to push the constraints on the cross-section below this value, excluding these WIMP scenarios. Note that for DM with mass, $m_\chi > 10$ GeV the thermal relic abundance constraint on the cross-section shows minor mass dependence [23].

We follow [23] when calculating the direct neutrino annihilation channel. In this case, the WIMP spin plays an insignificant role and hence can be neglected [19]. For indirect channels, we rely on the simulations performed in [24] for their neutrino production spectrum. The data released in [24] include various intermediate particle states, such as Ws, bs, and τ s, and their consequent decay products, e.g. neutrinos, electrons, etc. In section 2 and section 3, we give a thorough discussion of the signal and background modeling for P-ONE [1] and IceCube [25]. The final limits on the thermally averaged cross-section are shown in the section 4.

2 Signal modeling

This section briefly describes the calculation procedure for differential neutrino fluxes produced via DM annihilation measured by a neutrino telescope on Earth. The first subsection is dedicated to neutrino pair production from the galactic DM halo. In the second subsection, we discuss the modeling of an extra-galactic signal. We adopt the signal flux simulation described in [13, 26–28].

For this analysis, we consider DM self-annihilation to neutrino pairs, via a generic mass resonance, or W-boson and τ-leptons. Therefore, we developed a simulation software in which we can include various types of DM decay and annihilation channels(for example annihilation into W-bosons, b-quarks, etc.[1]). We compare the direct annihilation process as well as indirect channels via W-bosons and τ-leptons in section 4 with previous analyses.

2.1 Galactic contribution

In the case of direct annihilation, the galactic dark matter halo contributes trivially due to the negligible redshift. This means the flux spectrum arriving at Earth is almost identical to the spectrum at the production sites, given by eq. (2.1), assuming an equal neutrino flavor decomposition 1:1:1 after long-distance propagation

$$\frac{d\Phi_{\text{galactic}}}{dE} = \frac{1}{4\pi}\frac{\langle\sigma\nu\rangle}{\kappa m_\chi^2}\frac{1}{3}\frac{dN_\nu}{dE_\nu}J(\Omega). \tag{2.1}$$

$\langle\sigma\nu\rangle$ is the thermally averaged self-annihilation cross-section. We have used $\kappa = 2$ for Majorana DM with mass m_χ for the DM mass. The factor of 1/3 is due to equal distribution among neutrino flavors. dN/dE is the number spectrum of the neutrinos. Eq. (2.2) depicts the number spectrum of neutrinos produced via DM direct annihilation to neutrinos that

[1] https://github.com/MeighenBergerS/pone_dm/releases/tag/v1.0.0.

JCAP02(2024)049

have a typical delta peak

$$\frac{dN_\nu}{dE_\nu} = 2\delta\left(1 - \frac{E}{m_\chi}\right)\frac{m_\chi}{E^2}. \tag{2.2}$$

The spectrum shape varies depending on the annihilation channels. DM annihilation to W-boson pairs, b-quark pairs, and τ-lepton pairs are conventional choices. These heavy Standard Model (SM) particles can again decay into stable SM particles such as electrons, gamma-rays, or neutrinos. Modeling of the branching ratios is required to include different channels. In [24], thorough modeling has been performed using PYTHIA [29] and HERWIG [30] for the DM mass range from 100 GeV to 100 TeV.

For the direct annihilation to neutrinos, we neglect the Electroweak (EW) corrections. These would generate tails for the annihilation spectrum, increasing the yield of low-energy neutrinos and broadening the peak. As shown in [13, 26, 31–34], the broadening of the peak is less than 10%, which is well below the typical energy resolution for track-like events in IceCube [35]. These corrections would be significant in the case of cascade-like events, where the energy reconstruction is better. Of note, is that these corrections are relevant when considering other final states, such as γ, e^+, and $\bar{p}$, since these corrections induce a significant spectrum [33]. Contrary to the direct production channel, for the indirect channels, the EW corrections have been included in the spectrum from PPPC4DM [24]. In appendix A, we show the spectra for different annihilation channels.

The J in eq. (2.1), is the 'J-factor', which stands for the three-dimensional integration of the host galaxy's DM density ρ_χ over a solid angle Ω, within the line of sight $l.o.s.$

$$J(\Omega) = \int d\Omega \int_{l.o.s.} \rho_\chi^2(x) dx. \tag{2.3}$$

In the case of P-ONE, we use three distinct regions. The J-factor values are listed in table 1. In table 1 we give three J-factors: s-wave, p-wave, and d-wave. The s-wave corresponds to the thermally averaged cross section independent of velocity, p-wave to [$\langle\sigma\nu\rangle \propto (v/c)^2$] and d-wave [$\langle\sigma\nu\rangle \propto (v/c)^4$] each denoted as J_s, J_p, and J_d respectively. The p-wave and d-wave contributions are suppressed due to the typical Virial velocity of 100 km/s, hence, they can be neglected.The sensitivity region of the sky for different neutrino detectors affects the value of the integrated J-factor, as presented in [13, 26].

We modify the J-factor in IceCube's case, splitting it into northern (up-going) and southern (down-going) sky. We then focus on the up-going events, suppressing most of the atmospheric muon background. While this effectively removes most of this background, it also removes the galactic center from the field of view. Depending on the core or cuspy nature of the dark matter distribution, this can make a significant difference. Here, we use a cusped Navarro–Frenk–White (NFW) profile [36], which leads to a J-factor ~ 5 times smaller than the All-sky one shown in table 1 and [13, 26]. This results in a sensitivity drop of ~ 2. Note that using a different profile, such as an Einasto [37] or Burkert [38], leads to an approximately three times more or less stringent constraint, respectively. This has been widely studied in various previous works [19, 39, 40].

For the calculation of these J-factors, we assume the sun is located at a distance of $R_0 = 8.127$ kpc from the galactic center (GC), as determined by [11].

JCAP02(2024)049

Experiment	$J_s/10^{23}$	$J_p/10^{17}$	$J_d/10^{11}$
All-sky	2.3	2.2	3.6
Northern-sky	1.8	1.7	2.7
Southern-sky	0.5	0.5	0.9
P-ONE			
$cos(\theta) = [-1, -0.5]$	0.87	0.85	1.4
$cos(\theta) = [-0.5, 0.5]$	1.2	1.2	2.0
$cos(\theta) = [0.5, 1]$	0.13	0.12	0.18

Table 1. J-factors calculated using the NFW density profile [36], for IceCube (All-sky) and P-ONE [26]. The units of these J-factors are $\mathrm{GeV}^2\mathrm{cm}^{-5}\mathrm{sr}$. θ is the zenith angle. The columns are J-factors for the s-wave, p-wave, and d-wave contributions. For our analysis, we neglect the p-wave and d-wave contributions, due to their strong suppression.

The dark matter density used to calculate the J-factor in eq. (2.3) is parameterized as

$$\rho_\chi(r) = \rho_s \frac{2^{3-\gamma}}{(r/r_s)^\gamma (1 + r/r_s)^{3-\gamma}}. \tag{2.4}$$

Here, r is the distance from GC. We use the best-fit values from [41], with a local density of $\rho_0 = 0.4\,\mathrm{GeVcm}^{-3}$, a slope parameter $\gamma = 1.2$, and a scale density ρ_s at scale radius $r_s = 20\,\mathrm{kpc}$. Inverting eq. (2.4) and setting $\rho_\chi(R_0) \equiv \rho_0$ we obtain ρ_s. In figure 1 we show the differential neutrino flux at the earth, produced by DM annihilation with various masses from the galactic halo. There, we adopt $\langle\sigma\nu\rangle = 1 \times 10^{-23}\ \mathrm{cm}^3\mathrm{s}^{-1}$ and consider the neutrino production via DM annihilation to τ-pairs. The production spectra are taken from PPPC4DM [24].

2.2 Extra-galactic contribution

There are several approximation models for eq. (B.3). Here, we use the one described in [27]. We give a brief discussion of the different approximations in appendix B and appendix C along with a few intermediate results of our calculations. In figure 2, we show the flux results for two different DM indirect annihilation channels to neutrinos, τ-lepton(upper) and b-quark(bottom). Here we have used $\langle\sigma\nu\rangle = 3 \times 10^{-26}\ \mathrm{cm}^3\mathrm{s}^{-1}$ for comparing the flux results with figure5 in reference [42]. There is a factor of 10 difference between our results and the [42] flux, which can be explained due to differences in the approximation methods. Additionally, [42] mentioned they were using redshifts up to z = 49 in their simulations, which differ from our calculations. Even using the higher fluxes from [42], does not change the final CL limits significantly. For the direct annihilation channel to neutrinos, [26] showed that the extra-galactic flux would, at maximum contribute 10% to the final CL limit. We consider the 10% as an upper bound on contributions by extra-galactic sources. Although the possible extra-galactic contribution could vary between 0.0001% to 10% of the galactic one, it would at best minimally improve the final constraint value on the cross-section. Therefore, we neglect the extra-galactic component in the following analysis.

JCAP02(2024)049

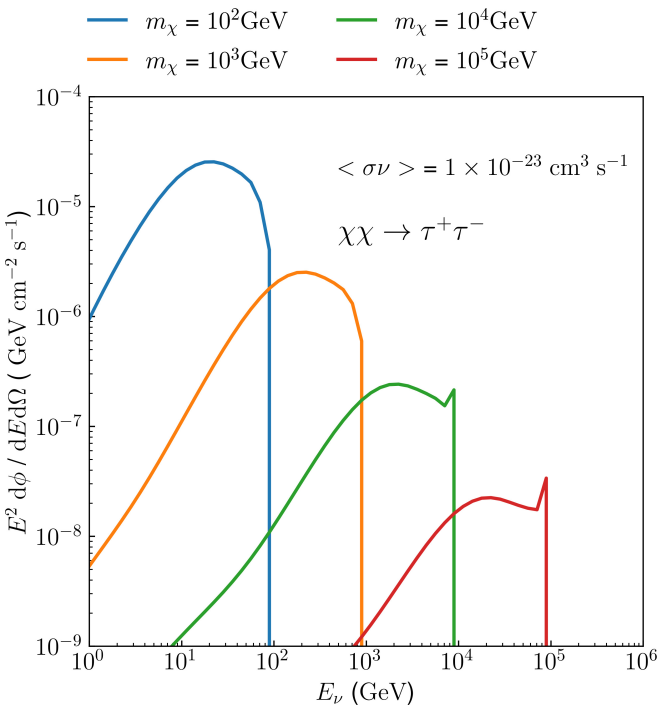

Figure 1. Differential neutrino fluxes for the galactic halo for various DM masses between 100 GeV and 100 TeV. Here $\langle\sigma\nu\rangle = 1 \times 10^{-23}$ cm^{3}s^{-1}, and the J-factors for P-ONE, see table 1, are used. The differential fluxes are calculated with the spectrum data from PPPC4DM [24] for DM annihilation to neutrino via the indirect τ-channel.

More analyses were done on extra-galactic contribution from the halo boost factor and halo substructures in [43] and [44]. According to [43], the total sub-halo contributions are dominant compared to those of smooth halo structures in the high mass regime, approximately above 10^4 GeV masses. In such scenarios, the contributions from extra-galactic sources boosted by substructures could be comparable with the galactic contribution. Future directional searches targeting nearby galaxies would be ideal for probing such substructure contributions further.

3 Effective areas and background

This section is dedicated to the effective areas of the IceCube and P-ONE observatories and the corresponding background fluxes. We describe the flux-to-count conversion with the help of effective areas since the later statistical analysis requires an event rate prediction.

The published IceCube effective areas [25] are binned with a zenith angle grid between 0° and 180°. In comparison, the simulated effective areas for P-ONE are differentiated into trimesters in the sky between 0° to 180°($-1 < \cos\theta < 1$). In figure 3, we show the effective areas for both P-ONE and IceCube. The solid line style corresponds to $-1 < \cos\theta < -0.5$, and the dashed-dotted to $-0.5 < \cos\theta < 0.5$. Note that the effective area line for $0.5 < \cos\theta < 1$ would overlap with the $-0.5 < \cos\theta < 0.5$ line. In addition to the effective area, in IceCube's case, we use the provided mixing matrices, to move from true neutrino energies to smeared energies. For P-ONE, we use the IceCube public energy smearing to approximate the energy reconstruction. The model is described at the end of this section. Observed and projected

JCAP02(2024)049

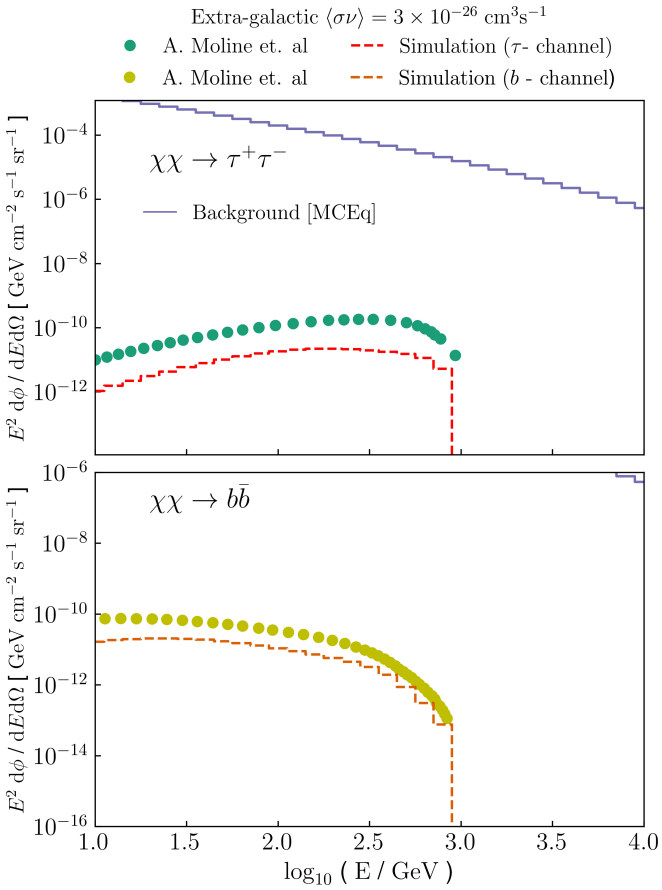

Figure 2. Differential neutrino fluxes of extra-galactic sources via in-direct annihilation of 10TeV-DM pairs into a $\tau^+\tau^-$ pair with $\langle\sigma\nu\rangle = 3 \times 10^{-26}$ cm^{3}s^{-1}. The difference in the flux results (dashed) compared to [42] (dotted) is due to uncertainties associated with the approximation methods. The blue line is MCEq simulated atmospheric neutrino background. Here we have parameterized the red-shift grid with the energy of neutrino at production E_{prod} and the mass of DM m_χ.

background counts are used for the likelihood analysis of the signal. To model the atmospheric background for P-ONE, we use MCEq [45], with the primary model H4a [46] and interaction model SYBILL2.3c [47]. Since the published effective areas are designed for track-like events, we will exclusively use ν_μ charged-current events.

Along with the atmospheric background, we have to include the astrophysical background for both detectors. We assume a power-law spectrum can model the astrophysical flux

$$\frac{d\Phi_{Astro}}{dE} = \phi_0 \times \left(\frac{E}{100\ \mathrm{TeV}}\right)^{-2.53\pm0.07}, \tag{3.1}$$

where we set the parameters to the best-fit values measured by IceCube, with a spectral index of 2.53±0.07 and $\phi_0 = 1.66^{+0.25}_{-0.27} \times 10^{-18}$ GeV cm^2 s sr^{-1} [48].

The differential fluxes for the background along with the signal fluxes for the galactic (eq. (2.1)) signals are then convolved with the effective areas of the neutrino detectors to produce the signal and background counts represented as N_{events} with t_{run} (run time of

JCAP02(2024)049

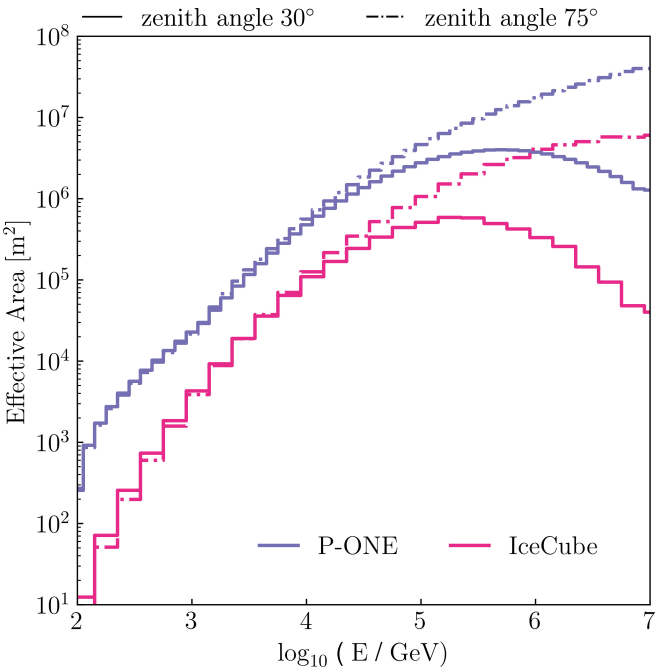

Figure 3. Effective area comparison between IceCube [25] and P-ONE [1] for zenith angles 30° and 75°. Due to the larger geometric volume, P-ONE will possess a larger effective area than IceCube. The solid line style corresponds to $-1 < \cos\theta < -0.5$, and the dashed-dotted to $-0.5 < \cos\theta < 0.5$. The effective area line for $0.5 < \cos\theta < 1$ would overlap with the $-0.5 < \cos\theta < 0.5$ line.

the detector) in eq. (3.2)

$$N_{events} = \iint \frac{d\Phi}{dE} \times A_{\text{eff}}(E, \theta, \phi) d\Omega dE \times t_{run}. \tag{3.2}$$

Using this energy-smearing procedure, we obtain the expected signal counts, depending on the dark matter mass and thermally averaged cross-section. Details on the energy smearing are given in appendix D. In figure 4 we compare ten years of observed IceCube events [25] with our predicted dark matter signals. Similarly, we show the expected background and dark matter to neutrino signal events after ten years for P-ONE in figure 5. There we give the results for an IceCube-like energy smearing (top) and a perfect detector (bottom). The energy smearing procedure is done with a log-normal distribution of events. This procedure is briefly explained in appendix D. The parameters used for the smearing are similar to the IceCube parameterization depicted in [35]. In figure 5, the smeared flux curves (upper graph) show changes in the energy distribution shape for different mass regimes. This is due to the different parameters according to their true energy region (resonant peaks with the DM mass) as discussed in appendix D.

4 Analysis and results

In this section, we perform a log-likelihood ratio test on IceCube data and predicted events for P-ONE. Both of these analyses were done with the NFW profile and combining the signal

JCAP02(2024)049

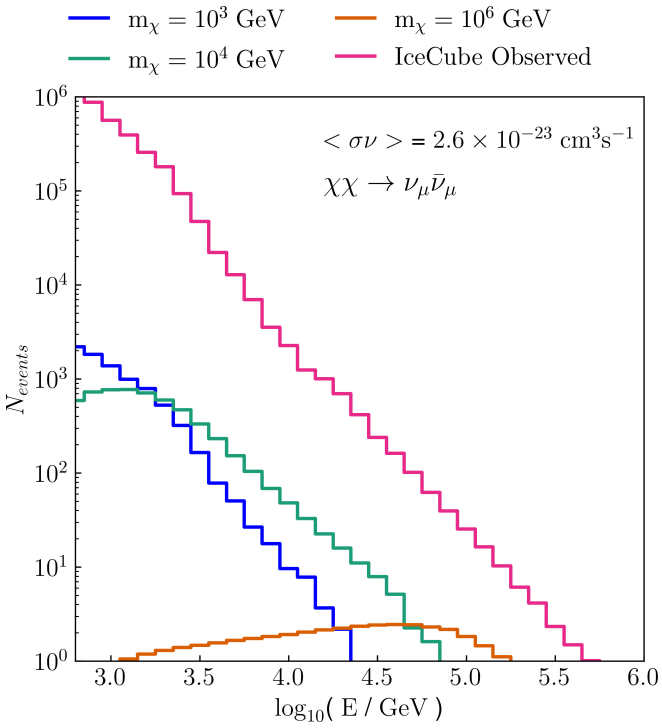

Figure 4. IceCube observed events (pink) and predicted signal counts with dark matter masses of 1 TeV (blue), 10 TeV (green), and 1 PeV (yellow). Here, the thermally averaged cross-section is $\langle\sigma\nu\rangle = 1 \times 10^{-23}$ cm^{3}s^{-1}.

fluxes as discussed in section 2 with galactic contributions. We define the binned likelihood function for the signal hypothesis, $\mathcal{H}_1$, to be

$$\mathcal{L}(\mathcal{H}_1)\& = \prod_i \mathcal{P}\left(d_i|\mu_{s,i}(\boldsymbol{\theta}) + \mu_{atmos,i}(\eta_1) + \mu_{astro,i}(\eta_2)\right) \tag{4.1}$$

The binning used for the background and signal distributions are the same. Here, $\mathcal{P}$ is a Poisson distribution, i runs over the energy bins, d_i is the measured event count taken from data and $\mu_{s,i}$ is the expected event count given the DM parameters $\boldsymbol{\theta}$. $\mu_{atmos,i}$ and $\mu_{astro,i}$ are the expected atmospheric and astrophysical events depending on nuisance parameters η_1 and η_2. For the astrophysical flux, η_2 is set to reflect the uncertainties on the parameters given in eq. (3.1), while for the atmospheric background, we assume a flat 20% uncertainty. A comparison between the CR, astrophysical flux uncertainties, and η_i, is shown in appendix F. We define the null hypothesis, $\mathcal{H}_0$, to have zero signal events ($\mu_{i,s}(\boldsymbol{\theta}) = 0$). We then define the test statistic q_μ as the log-likelihood ratio

$$q_\mu = -2\log\frac{\mathcal{L}(\mathcal{H}_1)}{\mathcal{L}(\mathcal{H}_0)}. \tag{4.2}$$

Since this is a diffuse analysis, we can disregard the right ascension of the events and create a background model by scrambling data in the right ascension. Note, that this reduces the sensitivity of this analysis since we remove any possible benefits from potential DM overabundance in the galactic center. To create the background model, we scrambled 10

JCAP02(2024)049

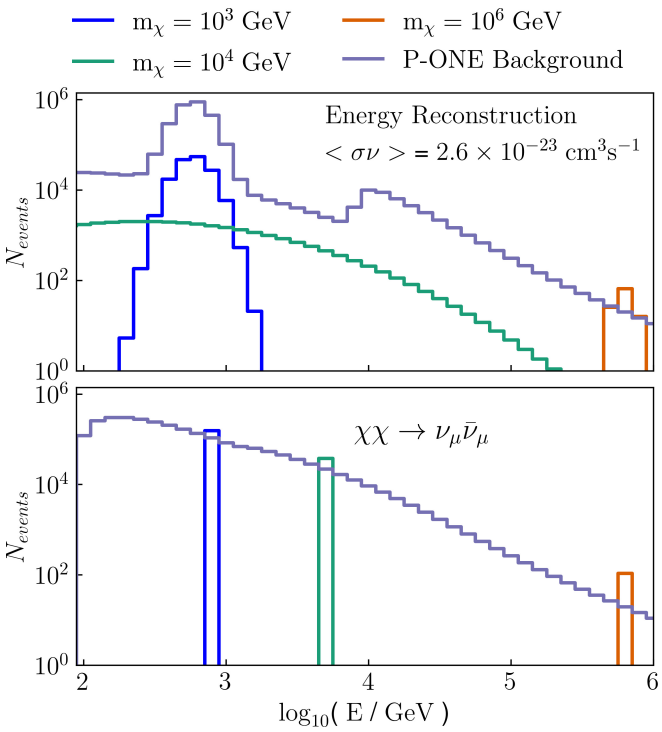

Figure 5. Expected counts for the P-ONE detector with ten years run-time for the direct DM to neutrino annihilation channel. The upper graph depicts expected counts with energy smearing. The bottom graph represents an ideal scenario with perfect energy reconstruction at the detector. The smearing parameters applied are similar to the IceCube public data energy smearing matrix from [35]. The 10^4 GeV peak seen in the fluxes is due to the parametrization we chose here.

years of IceCube data 10^6 times and constructed the mean binned in energy. Then we fit our atmospheric and astrophysical neutrino fluxes to the mean by scaling our calculations, see section 3. The scaling values are 1.1 for the atmospheric flux and 0.98 for the astrophysical flux. We then add the previously mentioned nuisance parameters η_1 and η_2 as floating normalizations to these best fits. We then follow [49] and marginalize over these parameters, to minimize the resulting limits. This is to account for the signal possibly contributing to the background.

In figure 6, we show the resulting confidence level (C.L.) limits for direct annihilation of DM pairs to $\nu_\mu\bar{\nu}_\mu$ using ten years of public IceCube data. The red solid curve represents the 95% C.L. sensitivity predicted in [26] for the high m_χ region with a Background Agnostic method. The green line shows the current bound set by KM3NeT [50] using a fraction of the planned detector. In yellow, we show the bounds set by ANTARES [51]. In appendix G, we compare these results to the expected ones, as well as a comparison of best-fit and injected background and signal events.

The strong bound set by ANTARES is due to its location and the analysis method. While far smaller than IceCube, the galactic center lies in ANTARES' most sensitive region. This allows ANTARES to perform a directional study of the galactic center, boosting its sensitivity. [52] shows that the location leads to approximately a factor of 20 sensitivity penalty for IceCube when performing similar analyses.

JCAP02(2024)049

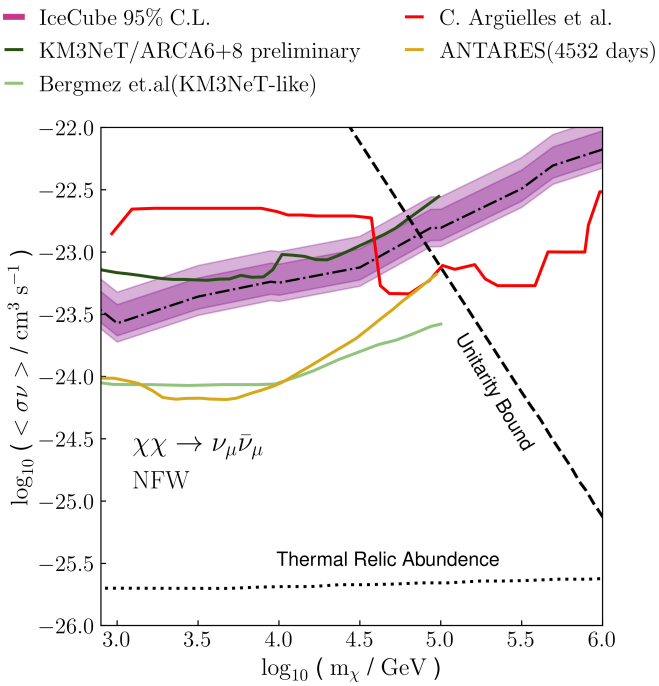

Figure 6. IceCube 95% C.L. limits using ten years of public data on the $\nu_\mu\bar{\nu}_\mu$ annihilation channel (black). The dark pink and light pink bands represent uncertainties due to the dark matter density and further model-related uncertainties. The solid red curve represents IceCube's high energy sensitivity estimate from [26] (red). The solid dark green and yellow curves are the current bounds set by KM3NeT [50] and ANTARES [51]. We also show light green curve for Bergmez et al. [39](KM3NeT-like), thermal relic abundance [23] (black dots), and the unitarity bound (black dashed).

In [39] the potential of a full KM3NeT-like [53] detector is shown calculated with an Angular Power Spectrum (APS) method assuming a run time of ten years. This would push the KM3NeT line below the ANTARES line.

We show the resulting predicted sensitivities for P-ONE in figure 7. The stark change in shape between 1 and 10 TeV mass is due to the energy-smearing model applied here. This change is especially relevant in the direct annihilation channel to neutrinos due to the expected peak at the mass resonance. If one removes our energy reconstruction assumptions, the P-ONE sensitivities will improve greatly, following a similar shape as the red line.

The P-ONE sensitivity could be improved by performing a spatial analysis similar to [39]. Purely from a scaling perspective, when comparing the effective areas, we would expect the P-ONE sensitivity to improve further by a factor between five and ten when utilizing spatial information.

In appendix E, we show example test statistic distributions and the resulting confidence limits for P-ONE and IceCube for the scanned model parameters, m_χ and $\langle\sigma\nu\rangle$.

We now analyze DM pair annihilation to W-bosons and consequent decay to muon neutrinos, depicted in figure 8. This analysis is done for the P-ONE detector with the numerical data from [24] assuming equilateral distribution amongst the flavors. The low energy cutoff was lowered to 500 GeV for this analysis. Our new limits (in the case of IceCube) are in energies above 1 TeV more stringent than previous analyses, e.g., IC86 by IceCube [54]. At the same time, we predict P-ONE's sensitivity using ten years of data to be even greater.

JCAP02(2024)049

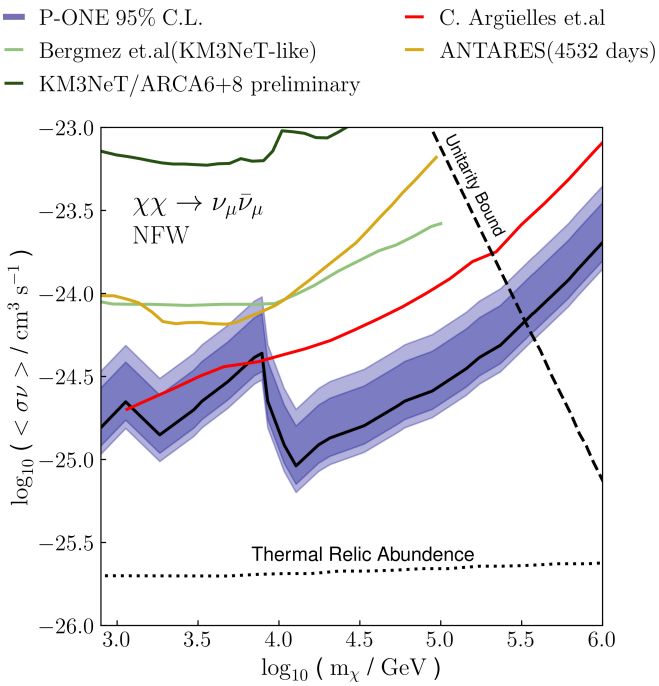

Figure 7. Sensitivity estimation for P-ONE. The solid black line shows the 95% C.L. limit. The 90% (dark blue) and 68% (light blue) bands represent uncertainties due to the dark matter density. The sensitivity is estimated with ten years of run-time, including energy smearing. The solid red curve represents the previous results from [26], the green curve represents the results from KM3NeT [50], and the yellow those from ANTARES [51]. We also show light green curve for Bergmez et al. [39](KM3NeT-like). The constraint linear shows a jump in the 10^3 GeV to $10^{3.7}$ GeV energy region. This is due to the log-normal distribution used in our P-ONE energy-smearing model (see appendix D).

Similarly, we have analyzed the τ-lepton channel for IceCube and P-ONE, with an NFW profile for $\nu_\mu\bar{\nu}_\mu$ pair production. Figure 9 shows the improvement between our results and the previous IC86 Galactic halo with all sky cascade signal [54] study.

In both annihilation scenarios, we expected P-ONE to outperform IceCube by an order of magnitude. The "jump" in the 10^3 to $10^{3.5}$ energy region which one can see in figure 7, is still present in figure 8 and figure 9. However, the jump is not as intense as it is for the direct channel since the neutrino spectrum is not a mass resonant peak rather, it is a distribution over the energy up to the dark matter mass discussed in figure 1.

Figure 9 shows that the projected P-ONE sensitivity to dark matter annihilation will exceed the constraints set by Fermi+MAGIC γ-ray limits for 15 dwarf satellite galaxies [55] in the high-mass region as well as exceeds that of predicted by ANTARES collaboration for 4532 days [51].

5 Conclusion

We performed dark matter annihilation searches on ten years of public IceCube data, setting the most stringent constraints on DM self-annihilation to neutrinos in the high-mass regime. Compared to previous analyses, the constraints set here also show almost one order of

JCAP02(2024)049

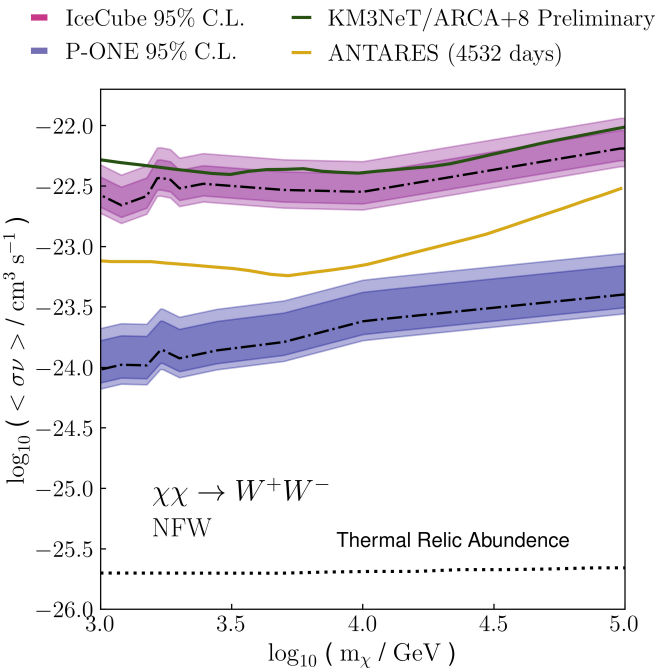

Figure 8. Thermally-averaged WIMP annihilation cross section as a function of the WIMP mass for W^+W- annihilation channels. The limits for IceCube (pink band) and estimated sensitivity P-ONE (purple band) are shown. Two W^+W- results from ANTARES(4532 days) [51] with yellow curve and KM3NeT/ARCA6 [50] are also presented as a comparison with dark green.

magnitude improvement to previous neutrino studies for the galactic halo, galactic center, and extra-galactic diffused sources in both the direct and indirect annihilation channels.

We also modeled sensitivities for a new proposed neutrino telescope, P-ONE. These show even greater potential than the constraints derived in this work for IceCube and can compete with constraints set by Fermi-LAT gamma-ray experiments. This indicates that P-ONE will play an important role in future DM searches, especially in the 10-100 TeV range.

We expect its detection potential could be pushed further toward the thermal relic abundance when performing an analysis similar to [39], which would include spatial information, unlike the diffuse analysis presented here. Directional information may become especially relevant when analyzing individual galaxies and studying sub-halo contributions [56] to the neutrino flux.

Acknowledgments

We thank Dr. Christian Haack and Dr. Martin Wolf for their valuable discussions, as well as Prof. Dr. Alejandro Ibarra and Dr. Shin'ichiro Ando for their guidance. Especially, We would also like to thank the support from Prof. Dr. Elisa Resconi. This research was supported by the German National Science Foundation (Deutsche Forschungsgemeinschaft, DFG) under the umbrella of the Special Research Activity (Sonderforschungsbereich, SFB1258) and the Australian Research Council's Discovery Projects funding scheme (Project DP220101727).

JCAP02(2024)049

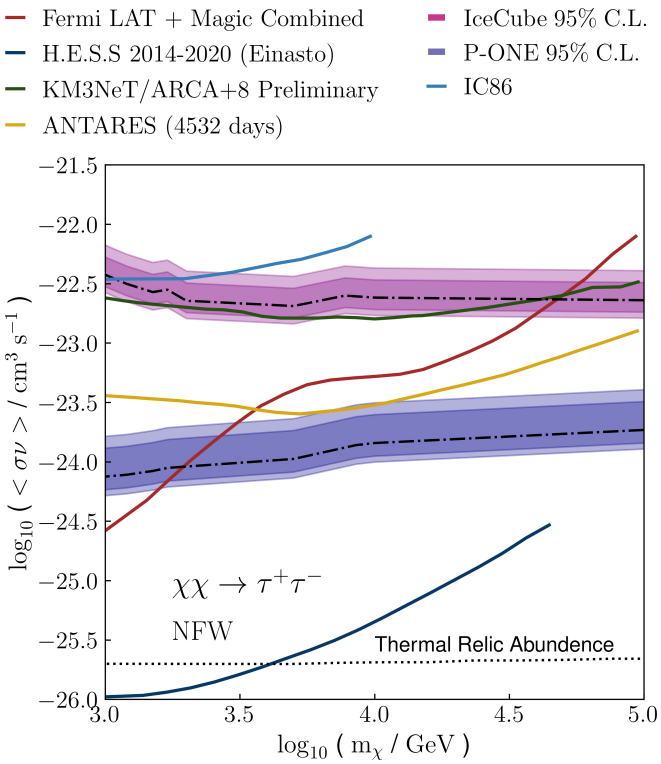

Figure 9. Thermally-averaged WIMP annihilation cross section as a function of the WIMP mass for $\tau^+\tau-$ annihilation channels. The limits for IceCube (pink band) and estimated sensitivity P-ONE (purple band) are shown. Several $\tau^+\tau-$ results from other neutrino experiments are shown: ANTARES [51](yellow) galactic plane search, IceCube 86 strings Galactic halo all-sky cascades [54] (blue) and KM3NeT/ARCA6 + 8 preliminary galactic center search [50] with dark green curve. The latest upper limits from gamma-ray combined searches by Fermi-LAT and MAGIC (brownish-red) on 15 dwarf satellite galaxies [55], H.E.S.S galactic center search [7] with dark blue curve.

A Spectrum for DM indirect annihilation channels

The spectrum data we used for indirect DM annihilation channels (at sources) are available at [24] and we show them in figure 1 The produced neutrinos are expected to have a long enough propagation distance so that after neutrino oscillation, they have a 1:1:1 flavor ratio at the Earth.

B Extra-galactic contributions

The extra-galactic flux is particularly interesting and rarely studied since the neutrinos produced in the extra-galactic sources would suffer non-negligible redshift effects. The neutrino flux from extra-galactic sources is calculated by eq. (B.1) for DM direct annihilation to the neutrino pair channel

$$\frac{d\Phi_{extra}}{dE_\nu} = \frac{1}{4\pi}\frac{\Omega_{DM}^2\rho_c^2\langle\sigma\nu\rangle}{\kappa m_\chi^2}\frac{1}{3}\int_0^{z_{up}} dz \frac{[1+G(z)](1+z)^3}{H(z)}\frac{dN_\nu}{dE_\nu}. \tag{B.1}$$

JCAP02(2024)049

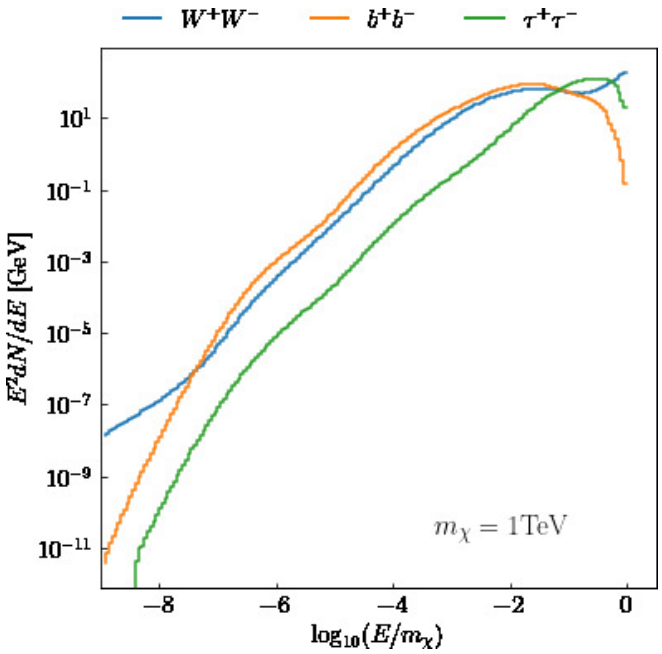

Figure 1. Energy spectrum E^2dN/dE respect to $x = E/m_\chi$) with $m_\chi = 10^3$ GeV. Shown are the W-boson (blue), b-quark (orange), and τ-lepton (green) channels.

Where $H(z) = H_0[(1+z)^3\Omega_m + (1+z)^4\Omega_r + \Omega_\Lambda]^{1/2}$ is the time-dependent Hubble parameter, ρ_c is the critical density of the Universe, and Ω_m, Ω_r, and Ω_Λ are, respectively, the fractions of ρ_c made up of matter, radiation, and dark energy [57]. The number spectrum of neutrino pair production is given in eq. (B.2)

$$\frac{dN_\nu}{dE_\nu} = 2\frac{m_\chi}{E'^2}\delta\left(\frac{m_\chi}{E'} - 1\right) = \frac{2}{E}\delta\left[z - (\frac{m_\chi}{E} - 1)\right], \tag{B.2}$$

which is similar to eq. (2.2). However, the redshift needs to be considered, which results in an energy transformation. The energy parameterization at Earth is $E = E'(1+z)$, with the energy at the source E' and the redshift, z, of the extra-galactic source. Similarly, the numerical spectra from [24] also require the transformation factor of $1/(1+z)$ for each energy bin.

$G(z)$ is the halo boost parameter at redshift z describing the clustering effect of matter in a galaxy's halo, given by

$$G(z) = \frac{1}{\Omega^2_{DM,0}\rho_c^2(1+z)^6}\int dM\frac{dn(M,z)}{dM}\int dr 4\pi r^2\rho^2_\chi(r). \tag{B.3}$$

With the halo boost, the DM annihilation rate has been parameterized with respect to redshift z and halo mass M. dn/dM describes the number distribution of halo masses and is strongly related to the halo mass function (HMF) [28]. A detailed discussion about its calculation is provided in appendix C. The selection of minimum halo mass affects the uncertainties of the final integral result. The smaller halos are more concentrated and contribute more to the neutrino flux, so choosing the lower integration bound is important. In this calculation, we set $M_{\min} = 10^{-3}M_\odot$ as a conservative lower limit [58, 59].

JCAP02(2024)049

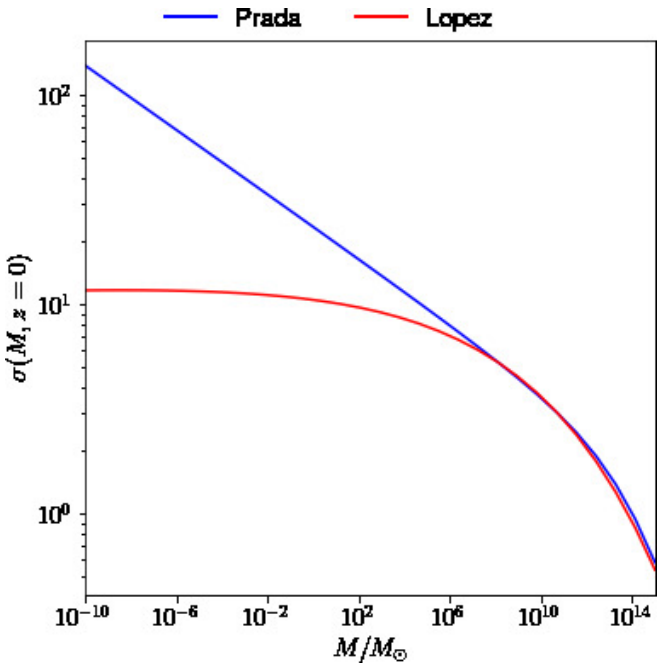

Figure 2. Dependence of the linear density field σ, on the Mass, M. The results from [60] and [27] have been compared here. The deviation is hard in the low halo mass region, whereas in the higher mass region, both approximations converge.

C Halo annihilation boost-factor

The halo boost factor G(z) depends on the halo mass function, which itself has a dependence on the variance of linear field density σ [60]

$$\sigma^2 = \Big(\frac{D(z)}{D(0)}\Big)^2 \int \frac{dk}{k} \frac{k^3 P(k)}{2\pi^2} |\tilde{W}(kR)|^2. \tag{C.1}$$

Eq. (C.1) defines the σ. The z dependence of σ is from the growth factor D(z) [60]. The $\tilde{W}$(kR) is the top-hat filter function and P(k) is the power spectrum. These two parts have only M dependence but not z. Therefore, we can treat M,z-dependence of σ separately. For $\sigma(M, z = 0)$ we use the parameterization described in the appendix of [27] and as in eq. (C.2):

$$\ln \sigma^{-1} = 0.2506(M^{0.07536} - 2.6M^{0.001745}). \tag{C.2}$$

The eq. (C.2) does not include the z dependence of σ. Its z dependence is introduced with the growth factor $D(z)$. In figure 2 we compared the approximation from [27] and from [60] at a wide mass range. At the higher mass, the two approximations converge. However, at the low mass region, there seems a significant divergence.

The mass function is non-trivially dependent on σ via function f(σ) as shown in eq. (C.3) [60]

$$\frac{dn}{dM} = f(\sigma) \frac{\rho_m}{M} \frac{d \ln(\sigma^{-1})}{dM}. \tag{C.3}$$

JCAP02(2024)049

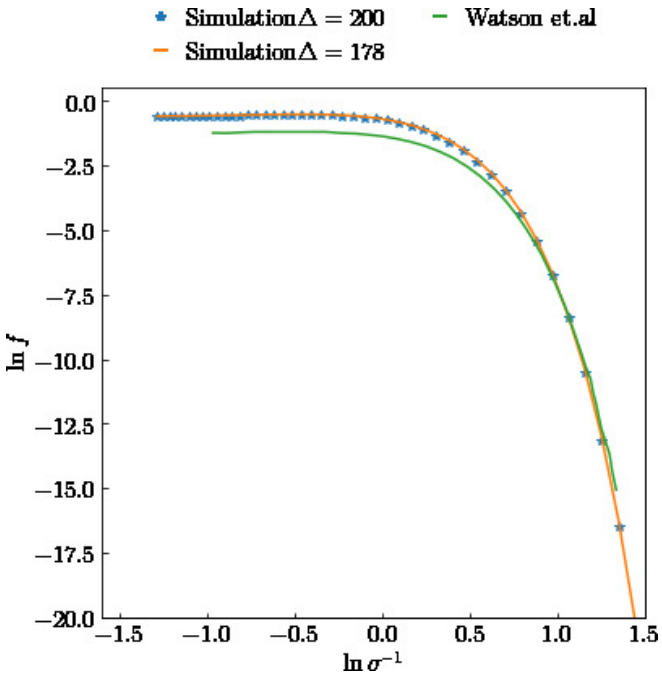

Figure 3. The fitted functions for the differential mass function f compared to σ at z=0 for both Δ parameters. The results from Watson et al. [28] and Lopez et al. [27] are within a difference of one order of magnitude.

$f(\sigma)$ function is called the differential mass function, which has various fitting methods developed over the years, as in [28, 61], and [62], etc. In our analysis, we used the approximation described in [27] because it is comparable with the results from [28], as shown in figure 3. The Δ symbol means the density described in terms of critical density ρ_c multiplied with a constant Δ.

The integral with ρ_χ(DM halo mass density) can be approximated by its concentration parameter $c = \frac{r_\Delta}{r}$ as in eq. (C.4):

$$\int_0^{r_\Delta} dr 4\pi^2 \rho_\chi^2(r) = \frac{M\Delta\rho_c(z)}{3}\tilde{g}(c_\Delta). \tag{C.4}$$

The integral has been described as a clumsiness factor in [63] or as an enhancement factor described in [64] as well as in [27]. The enhancement factor is dependent on the concentration parameter, c_Δ, and the halo mass, M. The $\tilde{g}$ has been approximated as eq. (C.5) [27]

$$\tilde{g}(c_\Delta) = \frac{c_\Delta^3}{3}\frac{[1-(1+c_\Delta)^{-3}]}{[\ln(1+c_\Delta) - c_\Delta(1+c_\Delta)^{-1}]^2}\,. \tag{C.5}$$

The concentration parameter can be bounded by the upper limit of 100, hence, one has a limit on the enhancement factor. There are several extensive models to approximate the concentration parameter described in [60, 65–67] and [68].

In our analysis, we have opted for the approximation of the concentration parameter c from [60]. The validity ranges over halo mass and redshift for various approximations change drastically, increasing the deviations even more. This results in larger differences

JCAP02(2024)049

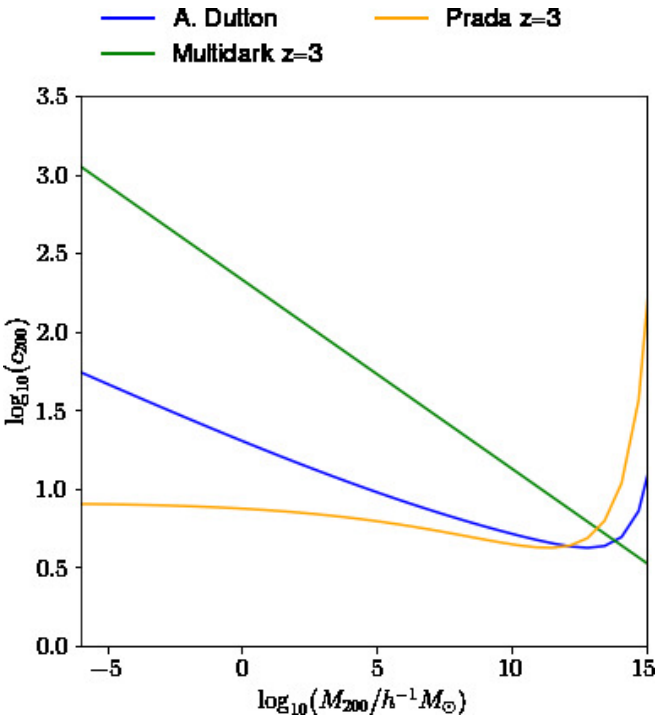

Figure 4. The concentration parameter comparison at z=3 throughout the halo mass for various models from [60, 65] and [69]. The approximations vary in the lower mass region by a greater margin. However, in the high-energy region, the variation is small.

in the estimations of halo boost factors and consequently affects the flux estimations. In figure 5 we compared the results of the halo boost factor with the approximation from [64] and simulation from [60].

The halo boost factor calculated from figure 5 will then be used in eq. (B.1) to calculate the differential flux.

D Smearing to approximate the energy reconstruction

The energy of an incoming particle (true energy) is converted into the optical module-registered photon. The reconstruction procedure converts the registered photon into an energy distribution. The process is specific to each detector. Since P-ONE is still in its early developing stage, we have used a log-normal distribution for the P-ONE energy reconstruction with the parameters close to the IceCube smearing matrix parameters published in [35]. With the help of eq. (D.1) we "reconstruct" the energy distribution of the detected neutrinos.

$$f(E_{\text{recon}}) = \frac{1}{\sigma\sqrt{2\pi}} e^{-\frac{(E_{\text{true}}-\mu)^2}{2\sigma^2}}, \tag{D.1}$$

The PDF describes the smeared energy(E_{recon}) distribution probability of each True energy (E_{true}) bin throughout the energy grid. The figure 6 shows the smeared energy distribution (E_{recon}) with respect to the true energy (E_{true}) with the parameters described in table 2. We are using three different "Energy Reconstruction" parameters from low to high energy

JCAP02(2024)049

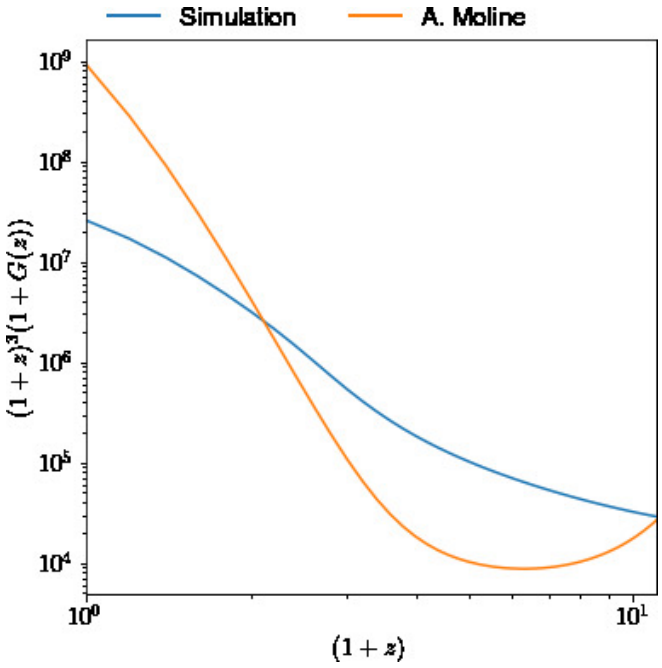

Figure 5. The halo boost factor G with respect to redshift z range (0, 20). A comparison between Prada et al. [60] simulated result and A. Moline et al. [64] simulated result is shown here. Both curves deviate to an even larger throughout the larger redshift range.

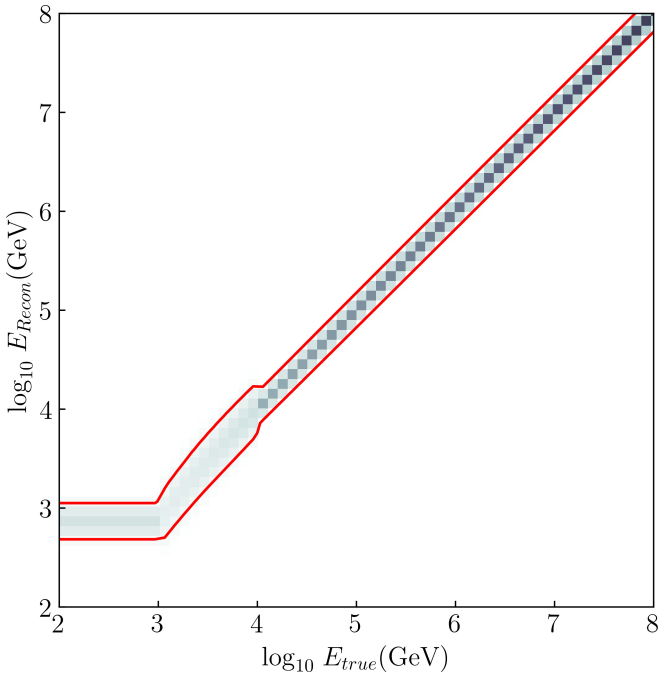

Figure 6. "Energy reconstruction" PDF used for P-ONE. It is a combination of log-normal distributions, with parameters shown in table 2. The color gradient of gray pixels presents the possibility of 0 (light) to 1 (dark) for a true energy to be reconstructed as the respective smeared energy. The red line indicates the 68% confidence interval.

JCAP02(2024)049

[TeV]	$E_{\text{true}} < 1$	$1 \leq E_{\text{true}} \leq 10$	$10 < E_{\text{true}}$
μ	0.7	linear spline	E_{true}
σ	0.45	linear spline	0.35

Table 2. Reconstruction parameters for P-ONE for different true energies given in TeV. The linear spline describes the linear extrapolation between the 1 TeV to 10 TeV boundaries.

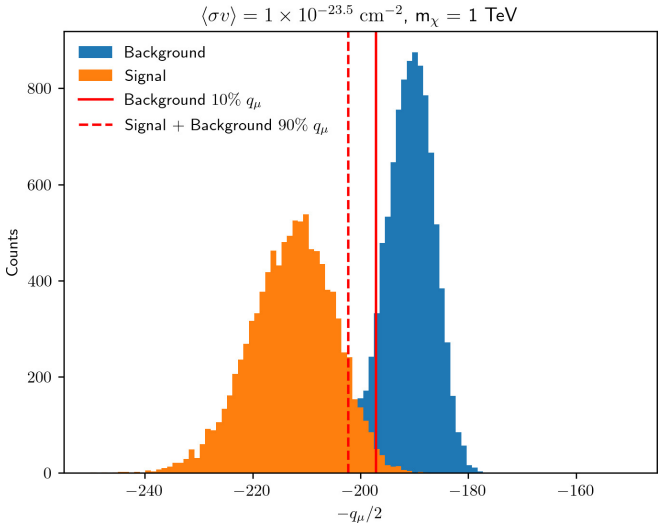

Figure 7. Example test statistic distributions for the background and signal hypothesis for IceCube. The red lines denote the 90% (dashed) and 10% (solid) quantiles for the signal and background hypothesis, respectively.

regions, i.e. below 1 TeV between 1–10 TeV and above 10 TeV. This is modeled in such a way to emulate "IceCube-like" energy smearing behavior as parameterized in [35]. In the figure 6, we see the log-normal distribution's behavior changing drastically from 10^3 GeV. This change results in the peak observed in the P-ONE limits between the energy band of 1 to 10 TeV. The decline from the peak also occurs due to a change in log-normal distribution at 10 TeV.

E Confidence level example

In figure 8 and figure 7, we show an example distribution of the test statistic for P-ONE and IceCube.

Figure 9 and figure 10 show the 95 % confidence levels (solid line) for P-ONE and IceCube respectively. This illustrates the distribution of confidence levels.

F Uncertainties due to atmospheric and astrophysical neutrino fluxes

In figure 11 we compare the uncertainties caused by CR and astrophysical neutrino uncertainties to the normalization uncertainties we introduce with η_1 and η_2. In the analysis range we consider here, CR and astrophysical uncertainties are smaller than those from η_1

JCAP02(2024)049

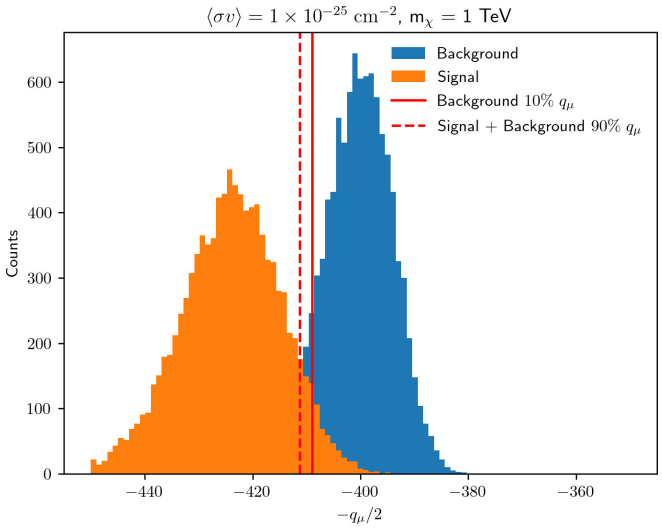

Figure 8. Example test statistic distributions for the background and signal hypothesis for P-ONE. The red lines denote the 90% (dashed) and 10% (solid) quantiles for the signal and background hypothesis, respectively.

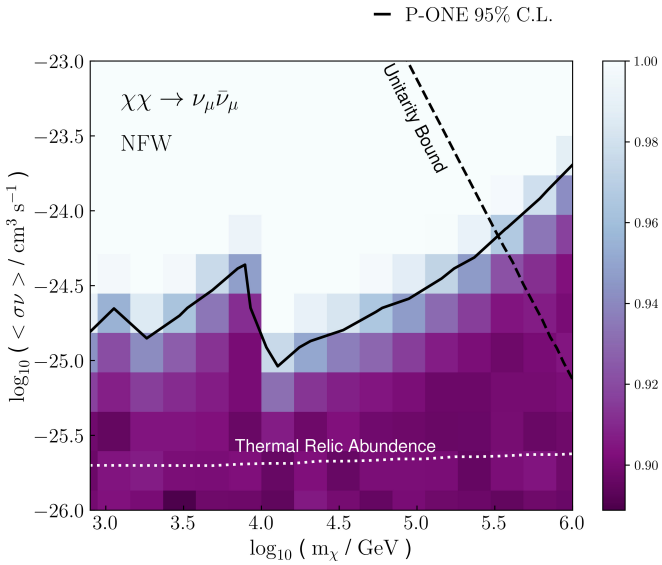

Figure 9. The confidence level plot for P-ONE. We have drawn the 95% confidence level contour for reference.

and η_2. The uncertainties from the CR flux are calculated by injecting different primary cosmic ray models, from [70].

G Analysis tests

In this section, we test the analysis method employed here. In figure 12 we compare the injected counts with the obtained best-fit values.

In figure 13, we compare the expected limit to the one set using IceCube data.

JCAP02(2024)049

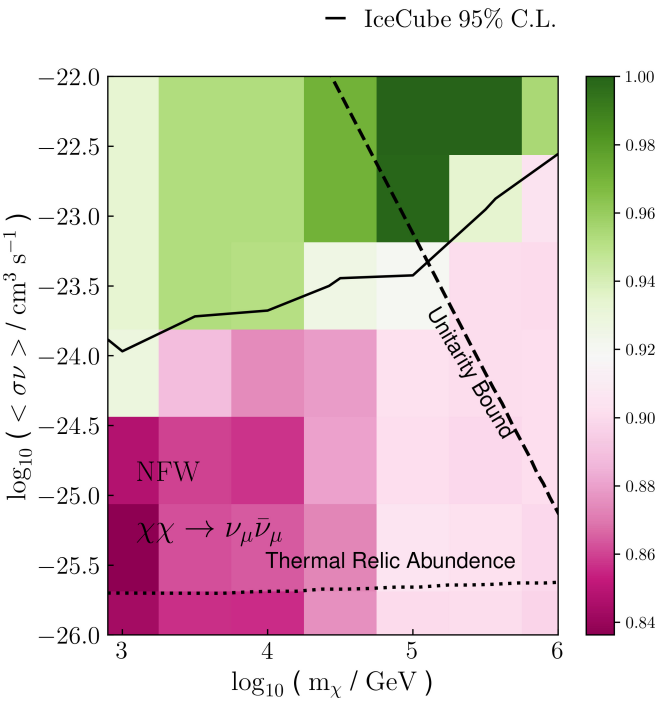

Figure 10. The confidence level plot for IceCube. We have drawn the 95% confidence level contour for reference.

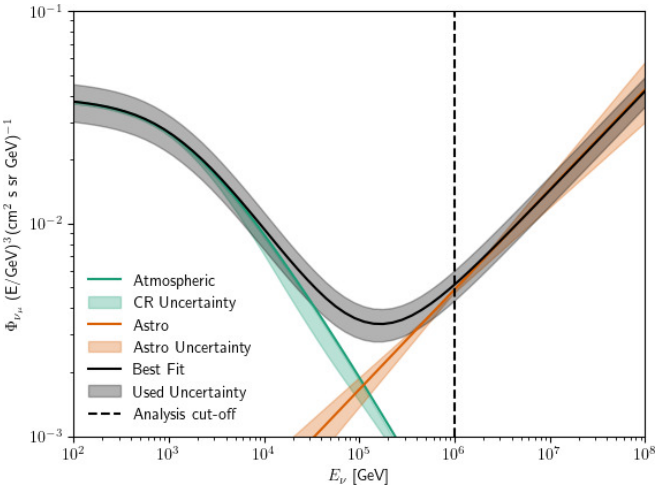

Figure 11. Here we show the uncertainties due to the cosmic ray flux (green) and the astrophysical neutrino flux (orange). We compare these uncertainties to the effects of η_1 and η_2 (gray) used in the analysis here.

JCAP02(2024)049

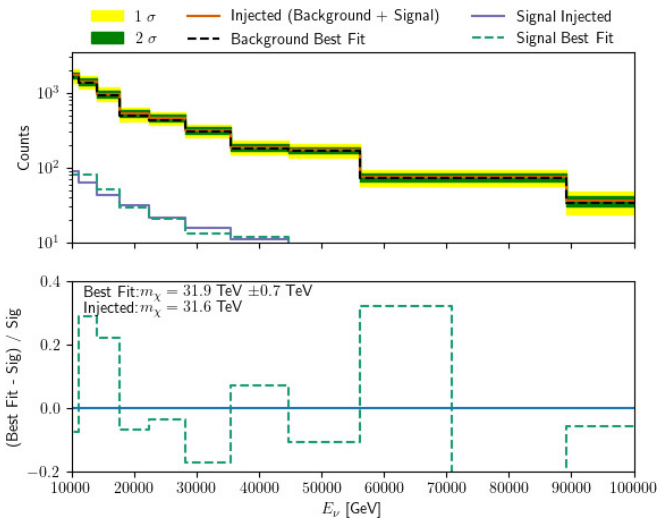

Figure 12. Comparing the injected signal and background (red) to the best-fit values for the background (black dashed) and signal (green dashed).

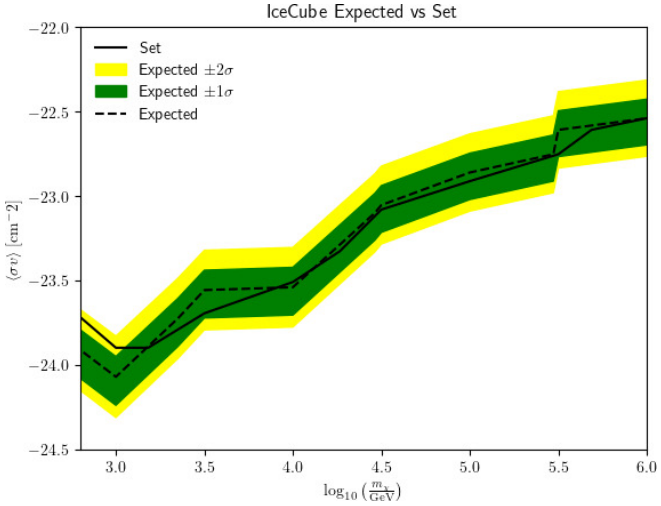

Figure 13. A comparison of the expected limit (dashed) to the one set using data (solid).

References

[1] P-ONE collaboration, *The Pacific Ocean Neutrino Experiment*, *Nature Astron.* **4** (2020) 913 [arXiv:2005.09493] [INSPIRE].

[2] KM3NeT collaboration, *KM3NeT: technical design report for a deep-sea research infrastructure in the Mediterranean sea incorporating a very large volume neutrino telescope*, (2009) [INSPIRE].

[3] Baikal-GVD collaboration, *Development of the double cascade reconstruction techniques in the Baikal-GVD neutrino telescope*, *PoS* **ICRC2021** (2021) 1167 [arXiv:2108.00333] [INSPIRE].

[4] IceCube-Gen2 collaboration, *IceCube-Gen2: the window to the extreme universe*, *J. Phys. G* **48** (2021) 060501 [arXiv:2008.04323] [INSPIRE].

[5] IceCube collaboration, *The IceCube neutrino observatory: instrumentation and online systems*, 2017 *JINST* **12** P03012 [arXiv:1612.05093] [INSPIRE].

JCAP02(2024)049

[6] ANTARES collaboration, *Nuclearite search with ANTARES*, 2021 *JINST* **16** C09010 [arXiv:2107.13479] [INSPIRE].

[7] H.E.S.S. collaboration, *Search for dark matter annihilation signals in the H.E.S.S. inner galaxy survey*, *Phys. Rev. Lett.* **129** (2022) 111101 [arXiv:2207.10471] [INSPIRE].

[8] IceCube collaboration, *Search for dark matter from the galactic halo with the IceCube neutrino telescope*, *Phys. Rev. D* **84** (2011) 022004 [arXiv:1101.3349] [INSPIRE].

[9] IceCube collaboration, *Search for dark matter annihilation in the center of the Earth with* 8 *years of IceCube data*, *PoS* **ICRC2019** (2020) 541 [arXiv:1908.07255] [INSPIRE].

[10] IceCube collaboration, *Search for annihilating dark matter in the Sun with* 3 *years of IceCube data*, *Eur. Phys. J. C* **77** (2017) 146 [*Erratum ibid.* **79** (2019) 214] [arXiv:1612.05949] [INSPIRE].

[11] GRAVITY collaboration, *Detection of the gravitational redshift in the orbit of the star S2 near the galactic centre massive black hole*, *Astron. Astrophys.* **615** (2018) L15 [arXiv:1807.09409] [INSPIRE].

[12] K. Murase and J.F. Beacom, *Constraining very heavy dark matter using diffuse backgrounds of neutrinos and cascaded gamma rays*, *JCAP* **10** (2012) 043 [arXiv:1206.2595] [INSPIRE].

[13] IceCube collaboration, *Searches for connections between dark matter and high-energy neutrinos with IceCube*, *JCAP* **10** (2023) 003 [arXiv:2205.12950] [INSPIRE].

[14] J.F. Beacom, N.F. Bell and G.D. Mack, *General upper bound on the dark matter total annihilation cross section*, *Phys. Rev. Lett.* **99** (2007) 231301 [astro-ph/0608090] [INSPIRE].

[15] A. Esmaili, S.K. Kang and P.D. Serpico, *IceCube events and decaying dark matter: hints and constraints*, *JCAP* **12** (2014) 054 [arXiv:1410.5979] [INSPIRE].

[16] M. Chianese, G. Miele, S. Morisi and E. Vitagliano, *Low energy IceCube data and a possible dark matter related excess*, *Phys. Lett. B* **757** (2016) 251 [arXiv:1601.02934] [INSPIRE].

[17] M. Chianese, G. Miele and S. Morisi, *Dark matter interpretation of low energy IceCube MESE excess*, *JCAP* **01** (2017) 007 [arXiv:1610.04612] [INSPIRE].

[18] A. Bhattacharya, A. Esmaili, S. Palomares-Ruiz and I. Sarcevic, *Update on decaying and annihilating heavy dark matter with the* 6*-year IceCube HESE data*, *JCAP* **05** (2019) 051 [arXiv:1903.12623] [INSPIRE].

[19] IceCube collaboration, *Search for dark matter annihilation in the galactic center with IceCube-*79, *Eur. Phys. J. C* **75** (2015) 492 [arXiv:1505.07259] [INSPIRE].

[20] WMAP collaboration, *Seven-year Wilkinson Microwave Anisotropy Probe (WMAP) observations: cosmological interpretation*, *Astrophys. J. Suppl.* **192** (2011) 18 [arXiv:1001.4538] [INSPIRE].

[21] D. Clowe et al., *A direct empirical proof of the existence of dark matter*, *Astrophys. J. Lett.* **648** (2006) L109 [astro-ph/0608407] [INSPIRE].

[22] G. Steigman and M.S. Turner, *Cosmological constraints on the properties of weakly interacting massive particles*, *Nucl. Phys. B* **253** (1985) 375 [INSPIRE].

[23] G. Steigman, B. Dasgupta and J.F. Beacom, *Precise relic WIMP abundance and its impact on searches for dark matter annihilation*, *Phys. Rev. D* **86** (2012) 023506 [arXiv:1204.3622] [INSPIRE].

[24] M. Cirelli et al., *PPPC* 4 *DM ID: a Poor Particle Physicist Cookbook for Dark Matter Indirect Detection*, *JCAP* **03** (2011) 051 [*Erratum ibid.* **10** (2012) E01] [arXiv:1012.4515] [INSPIRE].

JCAP02(2024)049

[25] IceCube collaboration, *IceCube data for neutrino point-source searches years* 2008–2018, arXiv:2101.09836 [DOI:10.21234/CPKQ-K003] [INSPIRE].

[26] C.A. Argüelles et al., *Dark matter annihilation to neutrinos*, *Rev. Mod. Phys.* **93** (2021) 035007 [arXiv:1912.09486] [INSPIRE].

[27] L. Lopez-Honorez, O. Mena, S. Palomares-Ruiz and A.C. Vincent, *Constraints on dark matter annihilation from CMB observations before Planck*, *JCAP* **07** (2013) 046 [arXiv:1303.5094] [INSPIRE].

[28] W.A. Watson et al., *The halo mass function through the cosmic ages*, *Mon. Not. Roy. Astron. Soc.* **433** (2013) 1230 [arXiv:1212.0095] [INSPIRE].

[29] T. Sjöstrand et al., *An introduction to PYTHIA* 8.2, *Comput. Phys. Commun.* **191** (2015) 159 [arXiv:1410.3012] [INSPIRE].

[30] M. Bähr et al., *Herwig++ physics and manual*, *Eur. Phys. J. C* **58** (2008) 639 [arXiv:0803.0883] [INSPIRE].

[31] J.R. Christiansen and T. Sjöstrand, *Weak gauge boson radiation in parton showers*, *JHEP* **04** (2014) 115 [arXiv:1401.5238] [INSPIRE].

[32] C.W. Bauer, N.L. Rodd and B.R. Webber, *Dark matter spectra from the electroweak to the Planck scale*, *JHEP* **06** (2021) 121 [arXiv:2007.15001] [INSPIRE].

[33] P. Ciafaloni et al., *Weak corrections are relevant for dark matter indirect detection*, *JCAP* **03** (2011) 019 [arXiv:1009.0224] [INSPIRE].

[34] IceCube collaboration, *Searches for connections between dark matter and high-energy neutrinos with IceCube*, *JCAP* **10** (2023) 003 [arXiv:2205.12950] [INSPIRE].

[35] IceCube collaboration, *Energy reconstruction methods in the IceCube neutrino telescope*, 2014 *JINST* **9** P03009 [arXiv:1311.4767] [INSPIRE].

[36] J.F. Navarro, C.S. Frenk and S.D.M. White, *The structure of cold dark matter halos*, *Astrophys. J.* **462** (1996) 563 [astro-ph/9508025] [INSPIRE].

[37] U. Haud and J. Einasto, *Galactic models with massive corona I. Method*, *Astron. Astrophys.* **223** (1989) 89 [INSPIRE].

[38] A. Burkert, *The structure of dark matter halos in dwarf galaxies*, *Astrophys. J. Lett.* **447** (1995) L25 [astro-ph/9504041] [INSPIRE].

[39] S. Basegmez Du Pree et al., *Robust limits from upcoming neutrino telescopes and implications on minimal dark matter models*, *JCAP* **05** (2021) 054 [arXiv:2103.01237] [INSPIRE].

[40] IceCube collaboration, *IceCube search for dark matter annihilation in nearby galaxies and galaxy clusters*, *Phys. Rev. D* **88** (2013) 122001 [arXiv:1307.3473] [INSPIRE].

[41] M. Benito, A. Cuoco and F. Iocco, *Handling the uncertainties in the galactic dark matter distribution for particle dark matter searches*, *JCAP* **03** (2019) 033 [arXiv:1901.02460] [INSPIRE].

[42] Á. Moliné et al., *Isotropic extragalactic flux from dark matter annihilations: lessons from interacting dark matter scenarios*, *JCAP* **08** (2016) 069 [arXiv:1602.07282] [INSPIRE].

[43] C. Okoli, J.E. Taylor and N. Afshordi, *Searching for dark matter annihilation from individual halos: uncertainties, scatter and signal-to-noise ratios*, *JCAP* **08** (2018) 019 [arXiv:1711.05271] [INSPIRE].

JCAP02(2024)049

[44] S. Basegmez Du Pree et al., *Robust limits from upcoming neutrino telescopes and implications on minimal dark matter models*, *JCAP* **05** (2021) 054 [arXiv:2103.01237] [INSPIRE].

[45] D. Heck et al., *CORSIKA: a Monte Carlo code to simulate extensive air showers*, FZKA-6019 (1998) [INSPIRE].

[46] T.K. Gaisser, *Spectrum of cosmic-ray nucleons, kaon production, and the atmospheric muon charge ratio*, *Astropart. Phys.* **35** (2012) 801 [arXiv:1111.6675] [INSPIRE].

[47] F. Riehn et al., *The hadronic interaction model SIBYLL 2.3c and Feynman scaling*, *PoS* **ICRC2017** (2018) 301 [arXiv:1709.07227] [INSPIRE].

[48] IceCube collaboration, *Characteristics of the diffuse astrophysical electron and tau neutrino flux with six years of IceCube high energy cascade data*, *Phys. Rev. Lett.* **125** (2020) 121104 [arXiv:2001.09520] [INSPIRE].

[49] J. Heinrich and L. Lyons, *Systematic errors*, *Ann. Rev. Nucl. Part. Sci.* **57** (2007) 145 [INSPIRE].

[50] KM3NeT collaboration, *Indirect search for dark matter with the KM3NeT neutrino telescope*, *PoS* **ICRC2023** (2023) 1377 [INSPIRE].

[51] ANTARES collaboration, *Dark matter searches with the full data sample of the ANTARES neutrino telescope*, *PoS* **ICRC2023** (2023) 1375 [INSPIRE].

[52] IceCube collaboration, *Time-integrated neutrino source searches with 10 years of IceCube data*, *Phys. Rev. Lett.* **124** (2020) 051103 [arXiv:1910.08488] [INSPIRE].

[53] KM3Net collaboration, *Letter of intent for KM3NeT 2.0*, *J. Phys. G* **43** (2016) 084001 [arXiv:1601.07459] [INSPIRE].

[54] IceCube collaboration, *All-flavour search for neutrinos from dark matter annihilations in the Milky Way with IceCube/DeepCore*, *Eur. Phys. J. C* **76** (2016) 531 [arXiv:1606.00209] [INSPIRE].

[55] MAGIC and Fermi-LAT collaborations, *Limits to dark matter annihilation cross-section from a combined analysis of MAGIC and Fermi-LAT observations of dwarf satellite galaxies*, *JCAP* **02** (2016) 039 [arXiv:1601.06590] [INSPIRE].

[56] S. Ando, T. Ishiyama and N. Hiroshima, *Halo substructure boosts to the signatures of dark matter annihilation*, *Galaxies* **7** (2019) 68 [arXiv:1903.11427] [INSPIRE].

[57] S.M. Carroll, *Spacetime and geometry: an introduction to general relativity*, Cambridge University Press, Cambridge, U.K. (2019) [DOI:10.1017/9781108770385] [INSPIRE].

[58] J.M. Cornell, S. Profumo and W. Shepherd, *Kinetic decoupling and small-scale structure in effective theories of dark matter*, *Phys. Rev. D* **88** (2013) 015027 [arXiv:1305.4676] [INSPIRE].

[59] I.M. Shoemaker, *Constraints on dark matter protohalos in effective theories and neutrinophilic dark matter*, *Phys. Dark Univ.* **2** (2013) 157 [arXiv:1305.1936] [INSPIRE].

[60] F. Prada et al., *Halo concentrations in the standard ΛCDM cosmology*, *Mon. Not. Roy. Astron. Soc.* **423** (2012) 3018 [arXiv:1104.5130] [INSPIRE].

[61] R.K. Sheth and G. Tormen, *An excursion set model of hierarchical clustering: ellipsoidal collapse and the moving barrier*, *Mon. Not. Roy. Astron. Soc.* **329** (2002) 61 [astro-ph/0105113] [INSPIRE].

[62] D.S. Reed et al., *The first generation of star-forming haloes*, *Mon. Not. Roy. Astron. Soc.* **363** (2005) 393 [astro-ph/0504038] [INSPIRE].

JCAP02(2024)049

[63] J.E. Taylor and J. Silk, *The clumpiness of cold dark matter: implications for the annihilation signal*, *Mon. Not. Roy. Astron. Soc.* **339** (2003) 505 [astro-ph/0207299] [INSPIRE].

[64] Á. Moliné, A. Ibarra and S. Palomares-Ruiz, *Future sensitivity of neutrino telescopes to dark matter annihilations from the cosmic diffuse neutrino signal*, *JCAP* **06** (2015) 005 [arXiv:1412.4308] [INSPIRE].

[65] A.A. Dutton and A.V. Macciò, *Cold dark matter haloes in the Planck era: evolution of structural parameters for Einasto and NFW profiles*, *Mon. Not. Roy. Astron. Soc.* **441** (2014) 3359 [arXiv:1402.7073] [INSPIRE].

[66] J.S. Bullock et al., *Profiles of dark haloes. Evolution, scatter, and environment*, *Mon. Not. Roy. Astron. Soc.* **321** (2001) 559 [astro-ph/9908159] [INSPIRE].

[67] A.D. Ludlow et al., *The mass-concentration-redshift relation of cold dark matter haloes*, *Mon. Not. Roy. Astron. Soc.* **441** (2014) 378 [arXiv:1312.0945] [INSPIRE].

[68] R.H. Wechsler et al., *Concentrations of dark halos from their assembly histories*, *Astrophys. J.* **568** (2002) 52 [astro-ph/0108151] [INSPIRE].

[69] A. Klypin et al., *MultiDark simulations: the story of dark matter halo concentrations and density profiles*, *Mon. Not. Roy. Astron. Soc.* **457** (2016) 4340 [arXiv:1411.4001] [INSPIRE].

[70] T.K. Gaisser, T. Stanev and S. Tilav, *Cosmic ray energy spectrum from measurements of air showers*, *Front. Phys. (Beijing)* **8** (2013) 748 [arXiv:1303.3565] [INSPIRE].

JCAP02(2024)049